

# Averaging techniques for OCT imaging

Maciej Szkulmowski\* and Maciej Wojtkowski

*Institute of Physics, Faculty of Physics, Astronomy and Informatics, Nicolaus Copernicus University, Grudziadzka 5,  
87-100 Toruń, Poland*

\*maciej.szkulmowski@fizyka.umk.pl

**Abstract:** State-of-the-art Fourier-domain optical coherence tomography (OCT) allows for the acquisition of up to millions of spectral fringes per second. This large amount of data can be used to improve the quality of structural tomograms after effective averaging. Here, we compare three OCT image improvement techniques: magnitude averaging, complex averaging, and spectral and time domain OCT (STdOCT). We evaluate the performance for images on both linear and logarithmic intensity scales and discuss their advantages and disadvantages. We propose the use of the STdOCT approach as it offers the best advantages. Applications to *in vivo* imaging and speckle reduction are presented.

©2013 Optical Society of America

**OCIS codes:** (170.4500) Optical coherence tomography; (170.3880) Medical and biological imaging; (100.2980) Image enhancement.

---

## References and links

1. D. Huang, E. A. Swanson, C. P. Lin, J. S. Schuman, W. G. Stinson, W. Chang, M. R. Hee, T. Flotte, K. Gregory, C. A. Puliafito, and J. G. Fujimoto, "Optical coherence tomography," *Science* **254**(5035), 1178–1181 (1991).
2. A. F. Fercher, C. K. Hitzenberger, G. Kamp, and S. Y. Elzaiat, "Measurement of intraocular distances by backscattering spectral interferometry," *Opt. Commun.* **117**(1-2), 43–48 (1995).
3. M. Wojtkowski, "High-speed optical coherence tomography: basics and applications," *Appl. Opt.* **49**(16), D30–D61 (2010).
4. P. Targowski, M. Iwanicka, L. Tymińska-Widmer, M. Sylwestrzak, and E. A. Kwiatkowska, "Structural examination of easel paintings with optical coherence tomography," *Acc. Chem. Res.* **43**(6), 826–836 (2010).
5. R. J. Zawadzki, B. Cense, Y. Zhang, S. S. Choi, D. T. Miller, and J. S. Werner, "Ultrahigh-resolution optical coherence tomography with monochromatic and chromatic aberration correction," *Opt. Express* **16**(11), 8126–8143 (2008).
6. B. Potsaid, I. Gorczynska, V. J. Srinivasan, Y. L. Chen, J. Jiang, A. Cable, and J. G. Fujimoto, "Ultrahigh speed spectral / Fourier domain OCT ophthalmic imaging at 70,000 to 312,500 axial scans per second," *Opt. Express* **16**(19), 15149–15169 (2008).
7. W. Wieser, B. R. Biedermann, T. Klein, C. M. Eigenwillig, and R. Huber, "Multi-megahertz OCT: high quality 3D imaging at 20 million A-scans and 4.5 GVoxels per second," *Opt. Express* **18**(14), 14685–14704 (2010).
8. M. Sylwestrzak, D. Szlag, M. Szkulmowski, I. Gorczynska, D. Bokowska, M. Wojtkowski, and P. Targowski, "Four-dimensional structural and Doppler optical coherence tomography imaging on graphics processing units," *J. Biomed. Opt.* **17**(10), 100502 (2012).
9. T. Klein, W. Wieser, R. Andre, T. Pfeiffer, C. M. Eigenwillig, and R. Huber, "Multi-MHz FDML OCT: snapshot retinal imaging at 6.7 million axial-scans per second," *Proc. SPIE* **8213**, 82131E, 82131E-6 (2012).
10. M. Szkulmowski, I. Gorczynska, D. Szlag, M. Sylwestrzak, A. Kowalczyk, and M. Wojtkowski, "Efficient reduction of speckle noise in optical coherence tomography," *Opt. Express* **20**(2), 1337–1359 (2012).
11. R. Leitgeb, C. K. Hitzenberger, and A. F. Fercher, "Performance of Fourier domain vs. time domain optical coherence tomography," *Opt. Express* **11**(8), 889–894 (2003).
12. A. Szkulmowska, M. Wojtkowski, I. Gorczynska, T. Bajraszewski, M. Szkulmowski, P. Targowski, A. Kowalczyk, and J. J. Kaluzny, "Coherent noise-free ophthalmic imaging by spectral optical coherence tomography," *J. Phys. D Appl. Phys.* **38**(15), 2606–2611 (2005).
13. P. H. Tomlins and R. K. Wang, "Digital phase stabilization to improve detection sensitivity for optical coherence tomography," *Meas. Sci. Technol.* **18**(11), 3365–3372 (2007).
14. M. Szkulmowski, A. Szkulmowska, T. Bajraszewski, A. Kowalczyk, and M. Wojtkowski, "Flow velocity estimation using joint spectral and time domain optical coherence tomography," *Opt. Express* **16**(9), 6008–6025 (2008).
15. A. Szkulmowska, M. Szkulmowski, D. Szlag, A. Kowalczyk, and M. Wojtkowski, "Three-dimensional quantitative imaging of retinal and choroidal blood flow velocity using joint spectral and time domain optical coherence tomography," *Opt. Express* **17**(13), 10584–10598 (2009).

16. M. Szkulmowski, I. Grulkowski, D. Szlag, A. Szkulmowska, A. Kowalczyk, and M. Wojtkowski, "Flow velocity estimation by complex ambiguity free joint spectral and time domain optical coherence tomography," *Opt. Express* **17**(16), 14281–14297 (2009).
  17. J. Walther and E. Koch, "Enhanced joint spectral and time domain optical coherence tomography for quantitative flow velocity measurement," *Proc. SPIE* **8091**, 80910L, 80910L-7 (2011).
  18. D. Bukowska, D. Ruminski, D. Szlag, I. Grulkowski, J. Wlodarczyk, M. Szkulmowski, G. Wilczynski, I. Gorczynska, and M. Wojtkowski, "Multi-parametric imaging of murine brain using spectral and time domain optical coherence tomography," *J. Biomed. Opt.* **17**(10), 101515 (2012).
  19. B. F. Kennedy, M. Wojtkowski, M. Szkulmowski, K. M. Kennedy, K. Karnowski, and D. D. Sampson, "Improved measurement of vibration amplitude in dynamic optical coherence elastography," *Biomed. Opt. Express* **3**(12), 3138–3152 (2012).
  20. J. W. Goodman, *Statistical Optics* (Wiley, 2000).
- 

## 1. Introduction

Optical coherence tomography (OCT) is a rapidly developing noninvasive, noncontact imaging technique for semitransparent samples found in many medical imaging applications [1–3] as well as industrial material studies [4]. OCT employs light with a low temporal and high spatial coherence to obtain images with an axial resolution on the order of a few micrometers [5]. Technological advances in light detectors and sources have allowed Fourier-domain OCT (FdOCT) configurations that accelerate data acquisition; hundreds of thousands or even millions of image lines per second can be collected for spectral OCT (SOCT) [6] and swept source OCT (SSOCT) [7], respectively. High-speed acquisition of three-dimensional images has thus brought about 4D imaging [8, 9]. In addition, the ability to acquire a large amount of data in a short time can be exploited to enhance the quality of two-dimensional cross-sectional images [10].

The quality of an OCT imaging system is usually described in terms of its sensitivity, defined as the lowest signal that can be detected over the noise floor [11]. In the optimal configuration, OCT systems are shot-noise limited and decreasing the contributions of other types of noise will therefore have little impact on the sensitivity. The signal can be amplified either by increasing the incident power or the exposure time of the detector. Unfortunately, the power is limited by safety norms in the field of biomedical imaging as well as the efficiency of the available light sources. Increasing the detector integration time also has several disadvantages: significant increases in the acquisition time causes interferometric fringe washout due to the inevitable drift of the initial phase caused either by setup instabilities or sample motion with respect to the scanning beam, and the fringe visibility diminishes because light scattered from distinct positions in the sample is integrated. Additionally, long acquisition times require detectors with a deep quantum well depth; otherwise the condition that the power from the reference arm of the interferometer is much higher than that from the sample arm may not be fulfilled. This, in turn, would lead to strong autocorrelation signals and reflections that blur the image [12]. For these reasons, most OCT systems acquire data at shortest available exposure time with the highest acceptable incident power and image quality is improved by data postprocessing.

A common approach to improving the quality of OCT images is to average over the data to form a single tomogram line. In an ideal case, the data to be averaged are acquired from the same position, but, in practice, the beam is moved continuously over the sample. However, in the case of dense scanning, structural information in consecutively acquired spectra is almost identical. Therefore, averaging leads to an improvement in the image quality of the final tomogram as it dampens all noise variance, including shot noise. If a proper data analysis method is chosen, structural elements of the sample previously hidden under the noise floor may appear. Additionally, since spectral fringe signals are acquired with short exposure times, the impact of fringe washout linked to the sample velocity with respect to the beam (either real or caused by the beam motion) is strongly reduced. Another advantage is that evolution of the sample state over time can be observed, leading to both a higher image quality and the ability to perform functional studies such as velocity detection. It has been

shown that averaging of the spectral fringe signals and complex-valued Fourier transforms of the spectral fringes give identical results [13]. Therefore, in this paper, we focus only on the averaging of the Fourier-transformed spectra (A-scans). To date, arithmetic averaging of A-scans (either complex signals or the magnitudes) have been proposed and implemented [13], but details of the averaging algorithms are rarely disclosed by authors utilizing averaging for image quality enhancement.

We propose here the use of spectral and time domain OCT (STdOCT) processing that has previously been used for Doppler [14–18] and elastography imaging [19] but can be regarded as averaging of the A-scans using Fourier transformations. We compare this approach with two more commonly used averaging techniques: complex-value averaging and magnitude-squared averaging. OCT tomograms are presented both on linear and logarithmic intensity scales. The logarithmic intensity scale is typically used for display images, as it emphasizes weak scattering, whereas the linear scale is more common in automatic image segmentation procedures. For quantitative comparisons, we consider four image quality metrics.

## 2. Theory

### 2.1. Image quality metrics

In the averaging process, we distinguish between an A-scan, a Fourier transform of one OCT spectrum, and a tomogram line, formed from one or multiple A-scans. A simplified overview of an OCT tomogram line can be understood as follows: from a background with a nonzero mean emerge higher amplitude signals corresponding to the reconstructed structure. In an ideal case, the background is homogeneously distributed over the entire A-scan. Both parts of the line are burdened by noise. This idea is presented schematically in Fig. 1. The aim of image quality enhancement is to make the signal distinguishable from the background. This can be achieved either by diminishing the noise variance or by increasing the difference between the mean signal and background values.

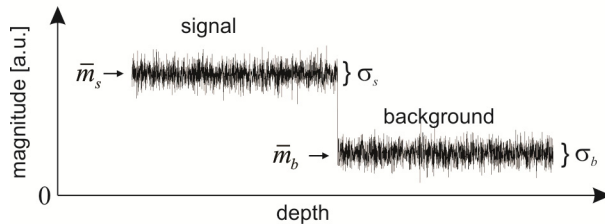


Fig. 1. Schematic drawing of the tomogram line with parameters used to calculate the image quality metrics:  $\bar{m}_s$  and  $\bar{m}_b$  are the mean values of the signal and background magnitudes in the presence of noise, respectively, and  $\sigma_s$  and  $\sigma_b$  are the corresponding standard deviations.

To quantitatively assess the image quality, we propose the following four parameters, which correspond to different image properties.

1. The signal-to-noise ratio (*SNR*):

$$SNR = \frac{\bar{m}_s}{\sigma_b}, \quad (1)$$

where  $\bar{m}_s$  is the mean value of the signal magnitude and  $\sigma_b$  is the standard deviation of the background.

2. The speckle contrast (*C*):

$$C = \frac{\sigma_s}{\bar{m}_s}, \quad (2)$$

where  $\sigma_s$  is the standard deviation of the signal magnitude.

3. The dynamic range ( $DR$ ):

$$DR = \bar{m}_s - \bar{m}_b, \quad (3)$$

where  $\bar{m}_b$  is the mean value of the background.

4. The contrast-to-noise ratio ( $CNR$ ):

$$CNR = \frac{\bar{m}_s - \bar{m}_b}{\sqrt{\sigma_s^2 + \sigma_b^2}}. \quad (4)$$

To optimize the performance of OCT imaging, the  $SNR$ ,  $DR$ , and  $CNR$  should all have the highest possible value. The speckle contrast  $C$  depends on the intensity fluctuations of the signal and should be minimized to achieve optimal performance. In the following, we present the probability density functions (PDFs) of the signal and noise-floor magnitudes for a single A-scan and tomogram lines after averaging with different techniques.

## 2.2. Single A-scan

Let us consider the complex-valued Fourier-transformed spectral fringe signal (the A-scan) to be composed of two components:

$$\Gamma^{(1)}(z) = \Gamma^c(z) + \eta^c(0, \sigma), \quad (5)$$

where  $\Gamma^c(z)$  is the signal of the one-dimensional sample structure, and the noise described by the complex function  $\eta^c(0, \sigma) = \eta_{re}(0, \sigma) + i \cdot \eta_{im}(0, \sigma)$ . Both the real and imaginary parts of the noise are different realizations of the same normal distribution with a zero mean and nonzero standard deviation  $\sigma$ . Following Goodman [20], for each depth position  $z$ , the coordinate system is chosen independently in such a way that the phase of the signal  $\Gamma^c(z)$  is equal to zero, thus making the signal real;  $\Gamma^c(z) = \Gamma(z) = s$ . Such an assumption simplifies further calculations. Taking into account that  $\eta(0, \sigma) + s = \eta(s, \sigma)$ , we can rewrite Eq. (5) in the form

$$\Gamma^{(1)}(z) = \eta_{re}(s, \sigma) + i \cdot \eta_{im}(0, \sigma). \quad (6)$$

To create a tomogram line, we calculate the magnitude-squared Fourier-transformed spectral fringes:

$$M^{(1)}(z) = |\Gamma^{(1)}(z)|^2 = \Gamma^{(1)}(z) \cdot \Gamma^{(1)*}(z). \quad (7)$$

To calculate the actual PDF of the magnitude of the tomogram line (or magnitude-squared A-scan), we use the same formalism as Goodman [20]:

$$p_M^{(1)}(m, s, \sigma) = \frac{1}{2\sigma^2} \exp\left\{-\frac{m+s^2}{2\sigma^2}\right\} I_0\left(\frac{\sqrt{ms}}{\sigma^2}\right), \quad (8)$$

where  $I_0(\cdot)$  is a modified Bessel function of the first kind, and  $m$  is the magnitude. In the following theoretical analysis, “magnitude” refers to a property of the tomogram lines and “magnitude-squared A-scan” refers to Eq. (7).

The mean value  $\bar{m}_{(1)}$  and variance  $\sigma_{(1)}^2$  of the PDF given in Eq. (8) can be calculated as

$$\bar{m}_{(1)} = s^2 + 2\sigma^2, \quad (9)$$

$$\sigma_{(1)}^2 = 4\sigma^2 (\sigma^2 + s^2). \quad (10)$$

At this stage, it is useful to stress the difference between  $\sigma$ , which is related to the real and imaginary parts of the complex-valued Fourier transform of the OCT spectrum, and the variance of the magnitude squared, which can be calculated from the tomogram line and used to compute the parameters given in Eqs. (1)–(4). Specifically, the parameter  $\sigma_{(1),s}^2 = \sigma_{(1)}^2$  can be calculated from parts of the image containing the signal and  $\sigma_{(1),b}^2 = 4\sigma^4$  can be computed from background (areas in which there is no signal). The PDF of the logarithm of the intensity  $L^{(1)}(z) = \log_{10} M^{(1)}(z)$  can be obtained by a simple variable transformation and is equal to

$$p_L^{(1)}(l, s, \sigma) = \frac{\ln 10}{2\sigma^2} \exp\left\{-\frac{10^l + s^2}{2\sigma^2}\right\} I_0\left(\frac{10^{l/2}s}{\sigma^2}\right) 10^l. \quad (11)$$

The mean value and variance of this PDF cannot be calculated analytically. Therefore, we compute them numerically using

$$\bar{x} = \int_{-\infty}^{\infty} x p_X(x) dx, \quad (12)$$

$$\sigma_X^2 = \int_{-\infty}^{\infty} (x - \bar{x})^2 p_X(x) dx, \quad (13)$$

where  $X$  is an arbitrary random variable.

### 2.3. Magnitude averaging

Averaging the magnitudes of the tomogram lines is the most logical way of processing the OCT data, as it has the clear advantage of being insensitive to phase instabilities. In the case of averaging  $N$  A-scans, the magnitude of the averaged tomogram line is given by

$$M^{(mag)}(z, N) = \frac{1}{N} \sum_{n=0}^{N-1} M_n^{(1)}(z). \quad (14)$$

For this type of averaging, the mean value remains the same, but the variance is divided by the number of averaged samples  $N$ :

$$\bar{m}_{(mag)} = \bar{m}_{(1)} = s^2 + 2\sigma^2, \quad (15)$$

$$\sigma_{(mag)}^2 = \frac{1}{N} \sigma_{(1)}^2 = \frac{1}{N} 4\sigma^2 (\sigma^2 + s^2). \quad (16)$$

The PDF of the magnitudes can be calculated by convolving the PDF given in Eq. (8)  $N$  times:

$$p_M^{(mag)}(m, s, \sigma, N) = \mathcal{F}^{-1} \left\{ \prod_{n=0}^{N-1} \mathcal{F} \left\{ p_M^{(1)}(m, s, \sigma) \right\} \right\}, \quad (17)$$

where  $\mathcal{F}$  and  $\mathcal{F}^{-1}$  are forward and inverse Fourier transformations, respectively. The PDF of the logarithm of the magnitude can be derived using a variable transformation that leads to the following expression:

$$p_L^{(mag)}(l, s, \sigma, N) = p_M^{(mag)}(10^l, s, \sigma, N) \cdot 10^l \ln 10. \quad (18)$$

#### 2.4. Complex averaging

For complex averaging of  $N$  A-scans, the magnitude of the averaged A-scans is given by

$$M^{(cpx)}(z, N) = \left( \frac{1}{N} \sum_{n=0}^{N-1} \Gamma_n^{(1)}(z) \right)^2, \quad (19)$$

where  $\Gamma^{(1)}(z)$  is a complex function given by Eq. (6). Complex averaging reduces the variance of both the real and imaginary parts of the complex signal without influencing their mean values. As a result, the PDF of the magnitude is similar to those given by Eq. (8) and Eq. (11), but the variance  $\sigma^2$  is divided by number of averaged complex signals  $N$ :

$$p_M^{(cpx)}(m, s, \sigma, N) = \frac{N}{2\sigma^2} \exp \left\{ -\frac{m+s^2}{2\sigma^2} N \right\} I_0 \left( \frac{\sqrt{ms}N}{\sigma^2} \right). \quad (20)$$

The mean value and variance of  $p_M^{(cpx)}(m, s, \sigma, N)$  are given by

$$\bar{m}_{(cpx)} = s^2 + 2 \frac{\sigma^2}{N}, \quad (21)$$

$$\sigma_{(cpx)}^2 = 4 \frac{\sigma^2}{N} \left( \frac{\sigma^2}{N} + s^2 \right). \quad (22)$$

The PDF of the magnitude on a logarithmic scale is given by

$$p_L^{(cpx)}(l, s, \sigma, N) = \frac{N \ln 10}{2\sigma^2} \exp \left\{ -\frac{10^l + s^2}{2\sigma^2} N \right\} I_0 \left( \frac{10^{l/2} s N}{\sigma^2} \right) 10^l. \quad (23)$$

#### 2.5. Spectral and time domain OCT

STdOCT has been described in detail in our previous work [14, 16]. A brief overview of the basic idea can be obtained by analyzing the data flow in the STdOCT diagram shown in Fig. 2, which shows the processing scheme used to create a single line of the tomogram. The data in each of the four panels is linked by a Fourier transformation (transformations from wavenumber space to depth position space occur from left to right, while temporal transformations to Doppler frequency space occur from top to bottom). The top-left panel (kt-plane) shows spectral fringes acquired in time by the FdOCT device. The number of horizontal lines in the diagram is equal to the number of spectra desired to create a single line in the final tomogram. Common FdOCT data processing flows can be presented as transforming data from the kt- to zt-plane via a spatial Fourier transformation followed by averaging the data in the zt-plane by using either the complex or magnitude approach.

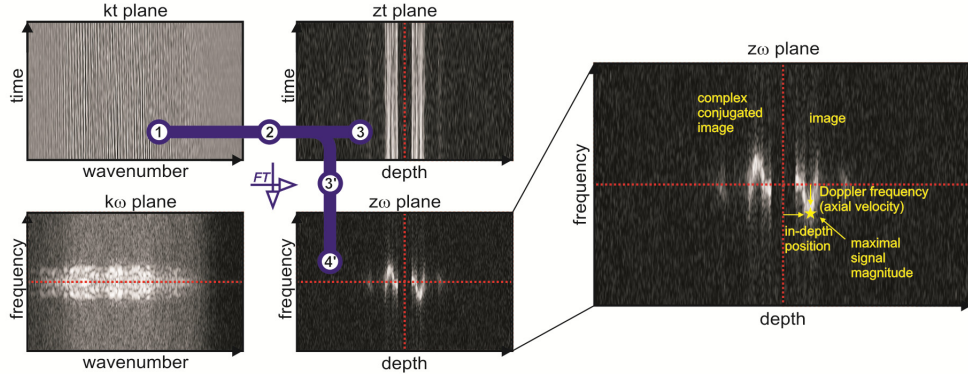


Fig. 2. STdOCT diagram indicating the order of procedures in data averaging for all three techniques. 1. Preprocessing (fixed-pattern noise reduction, resampling to wavenumber space, dispersion compensation). 2. Spatial Fourier transformation (FT) to in-depth position. 3. Magnitude or complex averaging. 3'. Temporal FT to Doppler frequency. 4'. Magnitude detection followed by information extraction in STdOCT processing. For each in-depth position, the signal with the maximum magnitude along the frequency axis is found. The magnitude value is used to create structural images, while the frequency value serves to create velocity maps.

In the STdOCT approach, data in the  $zt$  plane are transformed using a temporal Fourier transformation to the  $z\omega$ -plane, followed by the calculation of the magnitude

$$M^{(std)}(z, \omega, N) = \left( \frac{1}{N} \sum_{n=0}^{N-1} \exp[-i\omega t_n] \Gamma_n^{(1)}(z) \right)^2. \quad (24)$$

We note that the Fourier transformation is simply a weighted complex average computed for several different weights (dependent on the Doppler frequencies  $\omega$ ). For  $\omega=0$  complex averaging and STdOCT approach give identical results. The magnitude  $M^{(std)}(z, \omega, N)$  can be regarded as the distribution of Doppler frequencies in the in-depth position. This distribution changes if the sample has a velocity distribution. Therefore, the complete STdOCT procedure requires an additional step: for each in-depth position  $z$  in the  $z\omega$ -plane the magnitude of the signal at the center of the Doppler frequency distribution is found and used to create a pixel of the final tomogram line. Several approaches can be used to find this center [14, 17], but here we concentrate on the most straightforward method in which the maximum magnitude of the signal along the  $\omega$  axis is found:

$$M^{(std)}(z, N) = \max_{\omega} (M^{(std)}(z, \omega, N)). \quad (25)$$

To calculate the magnitude distribution obtained by the procedure given in Eq. (25), we assume that all the power of the signal is concentrated at one point in the Fourier transform given by Eq. (24); the remaining  $N-1$  points contain only noise. The PDF of the magnitude at the signal-dependent point is given by  $p_M^{(cpx)}(m, s, \sigma, N)$ , while the noise-related points have PDFs given by  $p_M^{(cpx)}(m, 0, \sigma, N)$ . The fact that the PDFs of the intensities are equal to the PDF of the complex-averaged amplitude is due to the Fourier transformation (Eq. (24)) being identical to complex averaging (Eq. (19)) since the weights only impact the phase of the averaged data.

To find the PDF of the maximum magnitude obtained using Eq. (25), we need to find the PDF of the maximum amplitude of the  $N-1$  data observations given by  $p_M^{(cpx)}(m, 0, \sigma, N)$

and one observation given by  $p_M^{(cpx)}(m, s, \sigma, N)$ . This can be calculated by multiplying  $N-1$  cumulative distribution functions (CDFs) of  $p_M^{(cpx)}(m, 0, \sigma, N)$  with one CDF of  $p_M^{(cpx)}(m, s, \sigma, N)$  and differentiating the result:

$$p_M^{(std)}(m, s, \sigma, N) = \frac{d}{dm} \left[ \left( \int_0^m p_M^{(cpx)}(m', 0, \sigma, N) dm' \right)^{N-1} \int_0^m p_M^{(cpx)}(m', s, \sigma, N) dm' \right]. \quad (26)$$

Although this is straightforward for the noise-floor background ( $s = 0$ ),

$$p_M^{(std)}(m, 0, \sigma, N) = \frac{N^2}{2\sigma^2} \exp \left[ -\frac{Nm}{2\sigma^2} \right] \left[ 1 - \exp \left[ -\frac{Nm}{2\sigma^2} \right] \right]^{N-1}, \quad (27)$$

it must be computed numerically in all other cases. The PDF of the logarithm of the magnitude can be found using a standard variable transformation [20]:

$$p_L^{(std)}(l, s, \sigma, N) = p_M^{(std)}(10^l, s, \sigma, N) \cdot 10^l \ln 10. \quad (28)$$

### 3. Methods and results

#### 3.1. Experimental setup and data processing

The experimental data were acquired and processed using the SOCT setup described in [10]. Briefly, the light source is a femtosecond Ti:Sapphire laser (Femtolasers Produktions GmbH, Austria) with a central wavelength of  $\lambda_0 = 795$  nm and a spectral width of  $\Delta\lambda = 155$  nm. The object arm is equipped with an retinal-imaging optical system with two optical galvanometric scanners and a 4-kHz resonant scanner for speckle averaging. The spectrometer uses a 1200 lines per millimeter (lpmm) diffraction grating (Wasatch Photonics, USA) and a complementary metal-oxide-semiconductor (CMOS) line scan camera (Basler AG, Germany). To allow imaging with speeds of up to 180,000 lines/s (5.5- $\mu$ s repetition time and 4.1- $\mu$ s exposure time), the CMOS detector is set to register 1280 pixels. Data processing for each spectrum consists of subtraction of the fixed-pattern noise, resampling from pixel-space to  $k$ -space (wavenumber space), numerical dispersion correction, spectral shaping, and Fourier transformation from wavenumber space to in-depth position space. As the last step, the spectra are averaged using one of the techniques discussed in the preceding section. All the steps are implemented with the use of the Intel Performance Primitives library and compiled with an Intel Compiler as a 64-bit multithreaded application. As the STdOCT algorithm involves a Fast Fourier Transform (FFT), this is the most time consuming averaging strategy. Current progress in developing parallel algorithms for OCT computational procedures is expected to allow for real-time STdOCT computation [8].

#### 3.2. Single reflector

For a FdOCT tomogram line reconstructed from experimental data, it is not possible to obtain direct values of the signal amplitude  $s$  and standard deviation  $\sigma$ . Instead, mean values of the magnitude of the background noise  $\bar{m}_b$  and signal areas  $\bar{m}_s$ , and the respective variances  $\sigma_b^2$  and  $\sigma_s^2$  are measured from the experimental data. The relations given in Eqs. (9), (10), (15), (16), (21), and (22) allow for the extraction of the signal amplitude  $s$  and standard deviation  $\sigma$  from this experimental data either by solving pairs of equations with respect to  $s$  and  $\sigma$  or by taking into account that the value of  $\bar{m}_b$  is obtained for  $s = 0$ . As a result,  $s$  and  $\sigma$  can be calculated using a variety of estimators created using these relations. With the aid of simulated data, we found that the estimators with the smallest variance are those calculated

from the magnitude-averaged data, i.e., using Eq. (15) ( $\bar{m}_{(mag),s} = s^2 + 2\sigma^2$  and  $\bar{m}_{(mag),b} = 2\sigma^2$ ):

$$s = \sqrt{\bar{m}_{(mag),s} - \bar{m}_{(mag),b}}, \quad (29)$$

$$\sigma = \sqrt{\bar{m}_{(mag),b}/2}. \quad (30)$$

An important property of these estimators is that their variances diminish as the number of averaged A-scans increases.

Using our SOCT setup, we performed an experiment for which a mirror is introduced into the object arm of the interferometer. Using the neutral density filter from the reference arm, we were able to change both  $s$  and  $\sigma$  in the resulting SOCT A-scans. We collected a data set of 700 000 spectra and averaged all the A-scans using magnitude averaging. Using the relations given in Eqs. (29) and (30), we obtained values of  $s = 0.327$  and  $\sigma = 0.200$ .

To compare the theoretical and experimental results, we divided the experimental A-scans into 2730 groups of 256 A-scans each. This allowed us to average the A-scans in each group with  $N$  ranging from 1 to 256 using all three averaging techniques and to create histograms of the magnitude. In the case of  $N=8$ , we generated PDFs of the magnitudes using the relations introduced in Section 2 with  $s$  and  $\sigma$  obtained from the experimental data. These PDFs are overlaid on the histograms of the magnitude created for the same averaging value in Fig. 3.

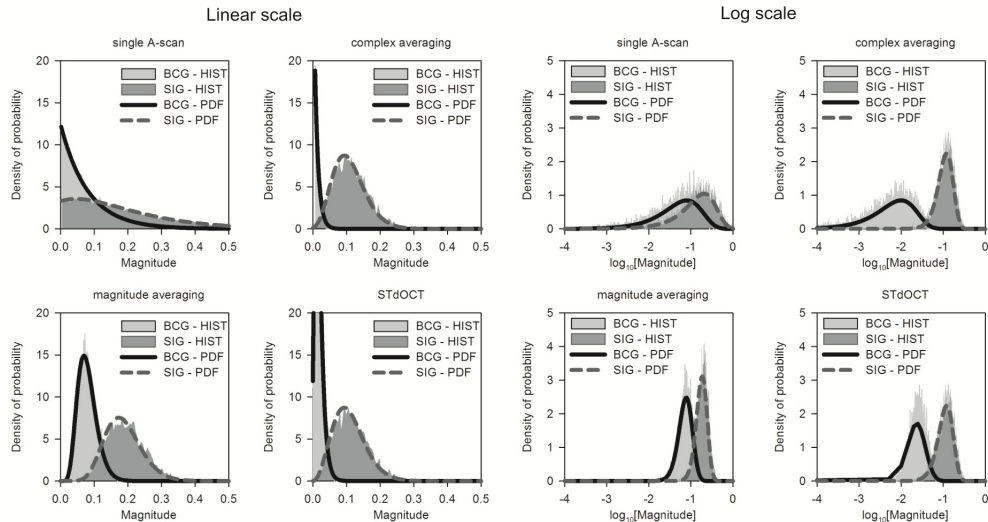


Fig. 3. Reflecting phantom experiment. PDFs and experimentally obtained histograms of the magnitudes of tomogram lines created with different averaging techniques for 8 averaged A-scans for a data set with  $s/\sigma = 1.635$ . *BCG - HIST*: histogram of the background magnitudes; *SIG - HIST*: histogram of the signal magnitudes; *BCG - PDF*: theoretical PDF of the background magnitudes; and *SIG - PDF*: theoretical PDF of the signal magnitudes.

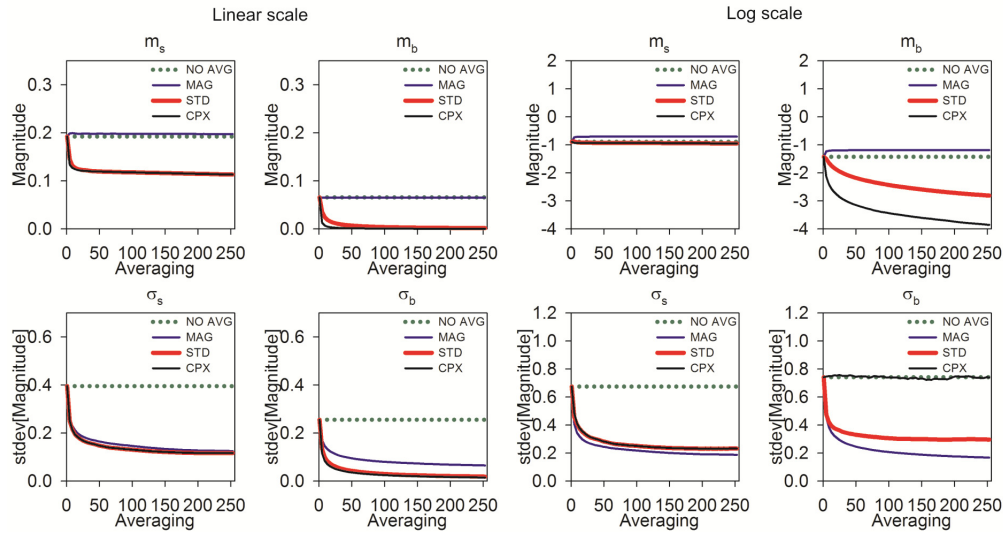


Fig. 4. Reflecting phantom experiment. Image parameters calculated from the magnitudes of the tomogram lines as a function of the number of averaged A-scans for different averaging techniques of a data set with  $s/\sigma = 1.635$ . Image parameters from left to right:  $\bar{m}_s$ : mean value of the signal;  $\bar{m}_b$ : mean value of the background noise;  $\sigma_s$ : standard deviation of the signal; and  $\sigma_b$ : standard deviation of the background noise.

It is not possible to numerically calculate the modified Bessel function  $I_0(\cdot)$  in Eqs. (8), (11), (18), (20), and (23) when the argument is larger than  $\sim 700$ , which means that the PDFs cannot be shown for all the desired number of averaged A-scans. Therefore, Fig. 3 shows the correspondence between the theoretical model and the experimental data, and in Fig. 4, we plot  $\bar{m}_s$ ,  $\bar{m}_b$ ,  $\sigma_s$ , and  $\sigma_b$  for tomogram lines on both linear and logarithmic scales calculated from the histograms of the magnitude using the relations given in Eqs. (12) and (13). As predicted from Eqs. (15) and (21), the mean values of the signal and background do not depend on the number of averaged A-scans in the case of magnitude averaging but do diminish for the other techniques due to the reduction in the noise variance. The standard deviation of the magnitude in all cases also diminishes as a function of the number of averaged A-scans. In terms of a logarithmic representation of the data, all the techniques have a similar effect on the mean value and standard deviation of the magnitude of the signal component of the tomogram line. The differences between techniques start to appear in the background component of the tomogram line. Magnitude averaging does not change the mean value but offers the highest reduction in the standard deviation. Complex averaging produces the opposite result. The STdOCT approach is the only technique that reduces both the mean value and standard deviation of the background noise in a logarithmic representation of the tomograms.

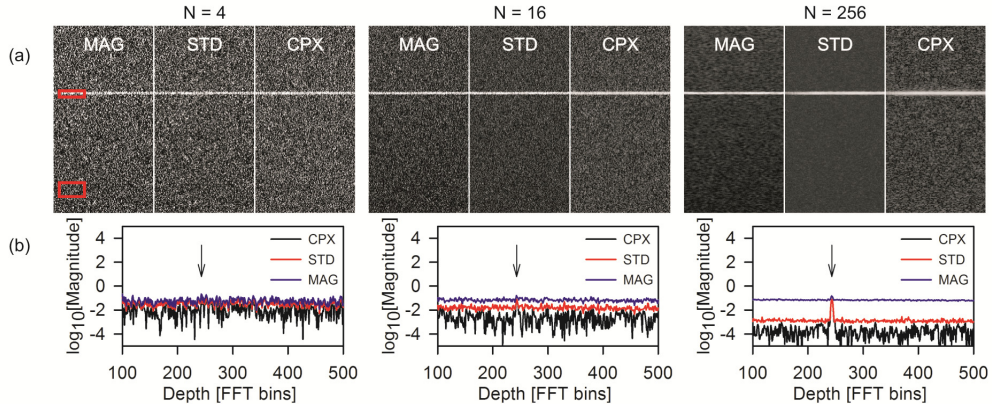


Fig. 5. (a). Images of the reflecting phantom for different averaging algorithms and number of averaged A-scans. Each tomogram is composed of 2 000 lines, and the dynamic range in all images is the same. Red rectangles indicate the regions of the tomograms used to calculate the image parameters in Fig. 6. For this data set,  $s/\sigma = 1.635$ . (b). Tomogram lines before dynamic range equalization taken from the images shown in (a). To emphasize the difference in the dynamic range, all the lines have equal maximal signal values. Arrows show the position of the reflecting layer. *MAG* : magnitude averaging; *STD* : STdOCT averaging; and *CPX* : complex averaging.

To visualize the impact of the extraction relations, we created tomograms of the reflecting phantom from the data used in the previous analysis for different numbers of averaged A-scans. Single tomogram lines are plotted in Fig. 5(b), and the increased dynamic range of the complex and STdOCT averaging techniques are clearly visible. The tomograms in Fig. 5(a) were created using all the averaging techniques with different numbers of averaged A-scans. To provide a fair comparison, the dynamic range of the images was equalized, which means that the intensity of all pixels is linearly remapped from  $m_{old}$  to  $m_{new}$  so that the mean values of the background  $\bar{m}_b$  and those in a chosen area containing the signal  $\bar{m}_s$  are equal in all the images:

$$m_{new} = \frac{m_{old} - \bar{m}_b}{\bar{m}_s - \bar{m}_b} \cdot 150. \quad (31)$$

Then, to quantify the change in the image quality observed in Fig. 5, we calculated the image parameters given in Eqs. (1)–(4) as a function of the number of averaged A-scans for each averaging technique. Mean values and standard deviations of the background and signal are computed from the areas indicated by the red squares in Fig. 5(a). These results are plotted in Fig. 6.

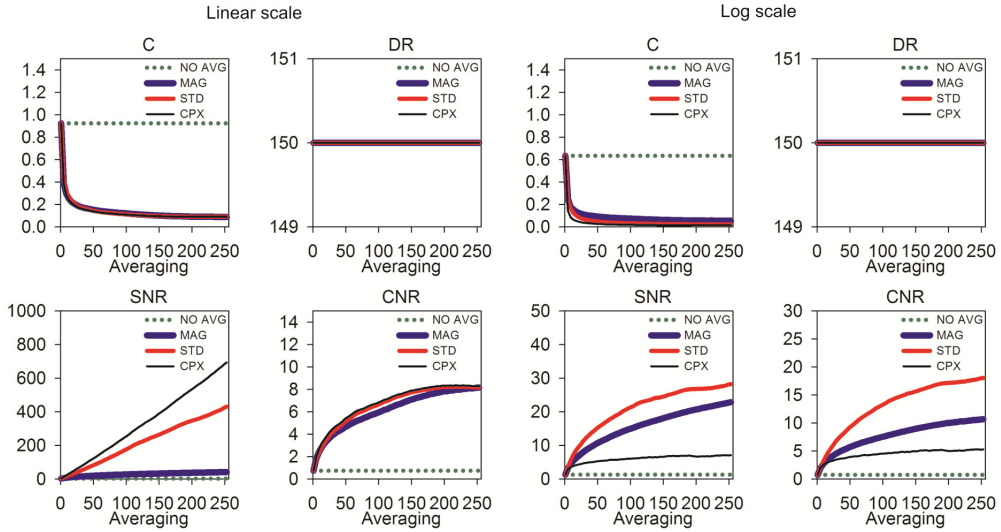


Fig. 6. Reflecting phantom experiment. Image quality metrics as a function of the number of averaged A-scans for different averaging techniques of a data set with  $s/\sigma = 1.635$ . The intensity of the tomogram used for the calculation was equalized, which results in a constant dynamic range.  $C$  : speckle contrast;  $SNR$  : signal-to-noise ratio;  $DR$  : dynamic range;  $CNR$  : contrast-to-noise ratio;  $NO\ AVG$  : single A-scan;  $MAG$  : magnitude averaging;  $STD$  : STdOCT averaging; and  $CPX$  : complex averaging.

After dynamic range equalization, on both linear and logarithmic scales, the contrast ( $C$ ) diminishes as the number of averaged A-scans increases. All the techniques perform similarly, with magnitude averaging achieving a slightly lower contrast. On the linear scale, the  $SNR$  and  $CNR$  are the highest for complex averaging, followed by those for STdOCT averaging. However, these relations change in a logarithmic representation of data: both the  $SNR$  and  $CNR$  are the best for STdOCT averaging, followed by magnitude averaging and complex averaging. The poor performance of complex averaging is due to the fact that on a logarithmic scale it does not offer any reduction in the background variance.

### 3.3. Scattering object

In SOCT imaging, due to light extinction, signals from deeper areas within the object becomes weaker until they completely vanish below the background noise level. From Fig. 5(b), it can be seen that the complex and STdOCT averaging techniques allow for a better imaging of objects with a low  $s/\sigma$  value. We expect that these techniques will therefore allow for the visualization of deeper structures than those possible with magnitude averaging. To investigate this hypothesis, we performed an experiment with a uniform-scattering phantom. Additionally, such an experiment give an insight into the behavior of the averaging techniques in the presence of speckle. Titanium dioxide distributed homogenously in an elastomer (polydimethylsiloxane (PDMS)) was used as the scattering object. During the acquisition, the beam was continuously scanned along a distance of 4 mm, and 10 000 spectra were acquired. The tomograms obtained by averaging the A-scans are presented in Fig. 7(a). Figure 7(b) presents a comparison of the single tomogram lines obtained with the three averaging techniques for different numbers of averaged A-scans. To preserve an identical lateral range in all the images, we averaged the A-scans using the sliding window approach with a window step of 5. The width of the incident beam was 12.7  $\mu m$ . The effective lateral resolution is decreased by the distance traveled by the beam during acquisition and is equal to approximately 14  $\mu m$  for  $N = 4$ , 19  $\mu m$  for  $N = 16$ , and 115  $\mu m$  for  $N = 256$ .

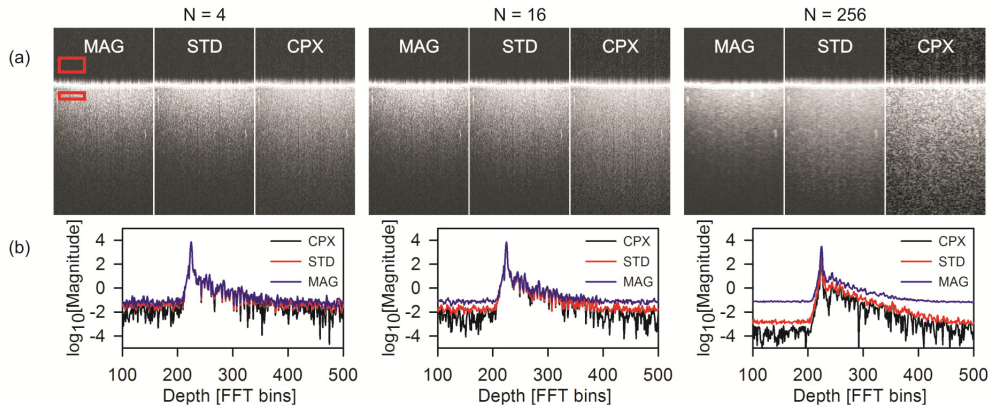


Fig. 7. (a). Images of the uniform-scattering sample for different averaging algorithms and number of averaged A-scans. The effective lateral resolution is 14, 19, and 115  $\mu\text{m}$  for  $N = 4$ , 16, and 256, respectively. The dynamic range in all images is equal. Red rectangles indicate the regions used to calculate the image parameters in Fig. 8. (b). Tomogram lines before dynamic range equalization of the images shown in (a). To emphasize the differences in the dynamic range, all the lines have equal maximal signal values. *MAG* : magnitude averaging; *STD* : STdOCT averaging; and *CPX* : complex averaging.

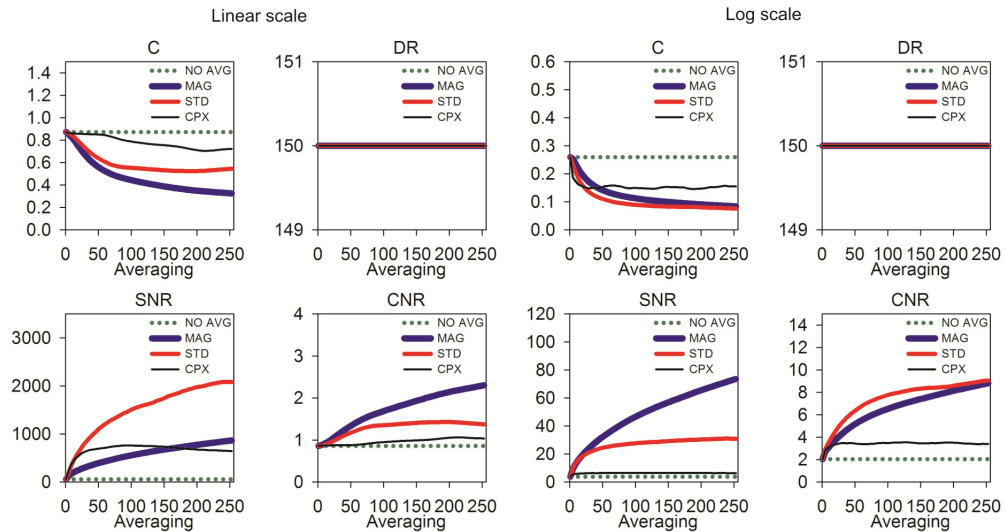


Fig. 8. Scattering phantom experiment. Image quality metrics as a function of the number of averaged A-scans for different averaging techniques. The intensity of the tomogram used for the calculation of the parameters was equalized and results in a constant dynamic range. *C* : speckle contrast; *SNR* : signal-to-noise ratio; *DR* : dynamic range; *CNR* : contrast-to-noise ratio; *NO AVG* : single A-scan; *MAG* : magnitude averaging; *STD* : STdOCT averaging; and *CPX* : complex averaging.

Figure 7(b) shows that in the case of imaging scattering samples, complex averaging, when compared to magnitude or STdOCT averaging techniques, still gives the highest gain in the dynamic range, allowing, in principle, the visualization of weakly scattering parts of the sample that are located at deeper positions in the sample, but this gain is compromised by higher speckle contrast and a lower contrast-to-noise ratio. When the magnitude and STdOCT averaging techniques are compared, although magnitude averaging gives a lower contrast and higher contrast-to-noise ratio on a linear scale and higher signal-to-noise ratio on a

logarithmic scale, the other parameters are better than those of STdOCT. These effects are visible also in Fig. 7(a), where the complex-averaged images suffer from high-contrast speckle noise. The magnitude-averaged and STdOCT images can also be seen to be of comparable quality, except that the STdOCT images offer a higher dynamic range allowing for the reconstruction of structures located deeper inside the sample.

Due to the movement of the probing light beam, the structure of the image differs between consecutive acquisitions of the spectral fringe signals. The phases of the complex A-scans cease to be identical, and complex-averaging leads to the creation of a new complex vector with a lower amplitude. In contrast, both magnitude averaging and STdOCT averaging are less susceptible to this effect due to the fact that both methods utilize the magnitudes of the complex vectors. Magnitude averaging is immune to phase variation as long as the amplitude of the averaged signals is nonzero. The STdOCT approach takes advantage of the fact that it calculates several complex averages of the spectral fringe signals with different complex weights, and from all of these complex averages, the technique picks the one with the highest magnitude. The maximum magnitude is detected independently for each in-depth position. As a result, the PDF of the magnitude is narrower and has a higher mean value. This leads to two important features. The first is that the pepper noise visible in the SOCT tomograms becomes almost invisible in the case of STdOCT averaging; the low intensity tail of the PDF makes the close-to-zero values improbable. The second feature is that the technique is almost insensitive to phase variations of the sample or decorrelation caused by shifting the beam on the sample. Even if the spectra are acquired from spatially separated areas of the sample, a nonzero magnitude is present. The latter property makes the STdOCT approach especially well suited to use in speckle-reduction techniques, as described in section 3.5. To quantify the image properties, we calculated the  $SNR$ ,  $C$ ,  $DR$ , and  $CNR$  values as a function of the number of averaged spectra. The mean values and standard deviations were taken from the areas indicated by the rectangles in the first tomogram in Fig. 7(a). The images underwent the same equalization procedure applied in the reflecting phantom imaging case. The image properties are presented in Fig. 8.

Comparing the results to those obtained for the reflector case, we immediately notice the worse performance of the complex-averaging technique across all parameters. In particular, the speckle contrast on both the linear and logarithmic intensity scales is higher than those of the magnitude- and STdOCT-averaging techniques. The sensitivity of complex averaging to decorrelation of the averaged spectra is visible in the plots of the contrast- and signal-to-noise ratios, where a “plateau” appears for  $N > \sim 30$ , for which the distance traveled by the beam ( $12 \mu\text{m}$ ) is similar to the size of the beam ( $12.7 \mu\text{m}$ ). This higher contrast in the signal component of the image is also visible in the plots of the  $SNR$ , where complex averaging gives a worse results than STdOCT, and in the case of logarithmic display, magnitude averaging. Plots of the  $CNR$  show that STdOCT and magnitude averaging increase the value of  $CNR$  to a greater extent than complex averaging.

#### *3.4. In vivo imaging*

To verify the performance of the averaging techniques in biomedical OCT imaging, we acquired 10 000 spectra from a 6 mm section of the human retina *in vivo*. The exposure time was set to  $4.1 \mu\text{s}$ , and repetition rate was  $5.5 \mu\text{s}$ . We scanned a distance of 6 mm through the center of the optic disc. The incident beam size was estimated to be  $\sim 8 \mu\text{m}$ . In Fig. 9, we present tomograms obtained from the same data set using different averaging techniques and two averaging values of  $N = 16$  and  $N = 64$ . The effective lateral resolution of the images includes the size of the beam and the distance traveled by the beam between the first and the last spectral acquisition. For  $N = 16$  and  $N = 64$ , the resolutions are  $17.6 \mu\text{m}$  and  $46.4 \mu\text{m}$ , respectively.

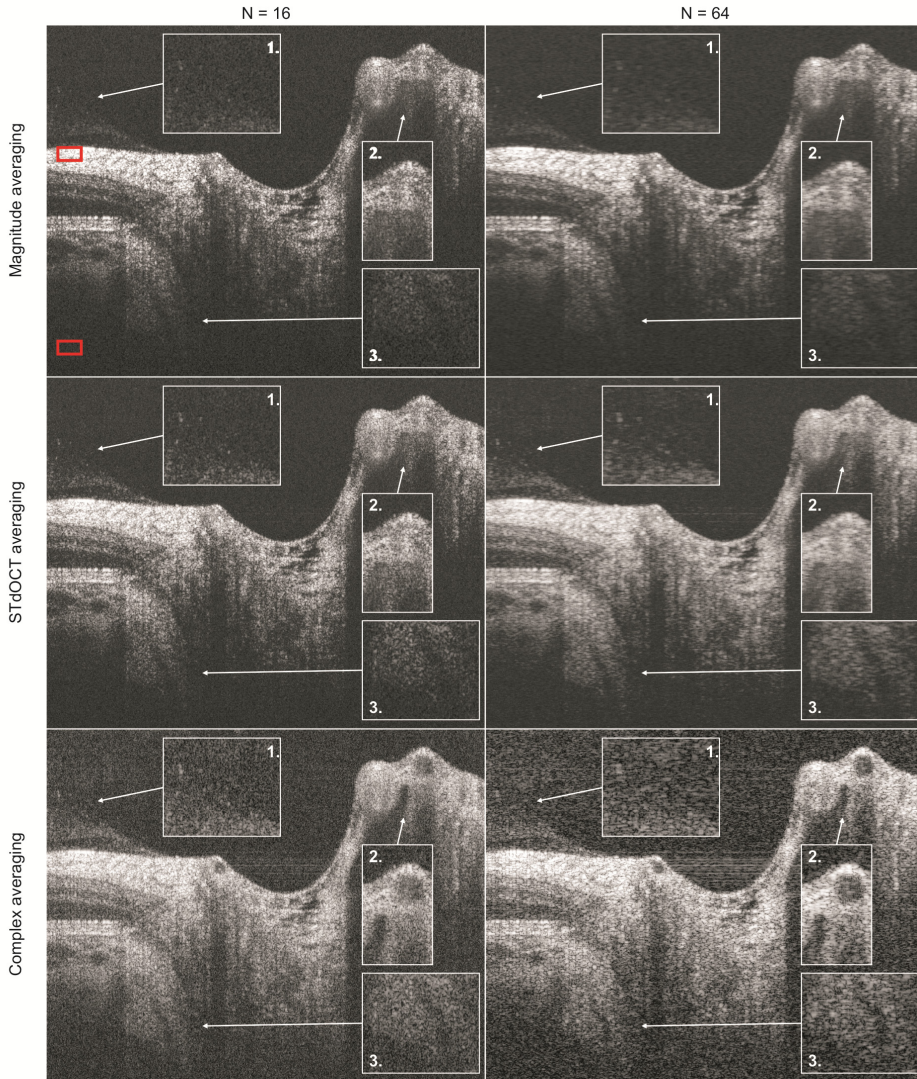


Fig. 9. In vivo imaging of a human optic nerve head. A total of 10 000 A-scans over a 6 mm lateral direction were obtained. The effective lateral resolution is  $17.6 \mu\text{m}$  and  $46.4 \mu\text{m}$  for  $N = 16$  and  $N = 64$ , respectively. Insets are magnified by 1.7 in both directions. 1. Vitreous humour. 2. Blood vessel. 3. Choroid.

In insets 1 and 3 in Fig. 9, we can see that for images obtained by averaging  $N = 16$  A-scans, the complex averaging technique enables visualization of weakly scattering structures in the vitreous humour and choroidal region. Additionally, this technique mainly increases  $DR$ , at the expense of a higher speckle contrast. In the case of a larger averaging,  $N = 64$ , complex averaging still offers the highest  $DR$ , but the high-contrast speckle blurs the fine retinal structures. Furthermore, the choroidal structures visible for the  $N = 16$  images start to vanish. This problem does not exist in the case of STdOCT imaging, where the choroidal and vitreous structures are more visible, speckle contrast is low, and  $DR$  is high. The additional advantages of the magnitude- and STdOCT-averaging approaches is that the fringe washout caused by movement of the sample is much weaker. This can be observed inside the retinal vessels (e.g., compare the insets labeled 2 in Fig. 9), where flowing blood disappears only in the case of complex averaging.

### 3.5. Application for speckle reduction

Speckle noise is caused by the interference of light reflected from scattering centers separated by subwavelength distances within the sample. If part of the signal from a scattering center contributes to interference in consecutive measurements of spectral fringes, then the fringes are correlated with the previous measurement and averaging partially reduces the contrast of the speckle pattern. Speckle noise is efficiently removed if the averaged A-scans are decorrelated. But, as mentioned in the previous section, decorrelated A-scans cannot be averaged using complex averaging; magnitude- or STdOCT-averaging approaches should be used. To demonstrate this, we applied our recently developed speckle reduction technique [10]. In this technique, the A-scans to be averaged are acquired at the same lateral position along the tomogram ( $x$ -direction) but the beam is deflected in a perpendicular direction ( $y$ -direction) by means of a rapidly oscillating resonant scanner. As a result, the distance traveled by the beam in the  $y$ -direction during collection is precisely controlled.

In the experiment, we imaged 6 mm through the center of a macula lutea. The distance traveled by the beam in  $y$ -direction was set to 110  $\mu\text{m}$ , which was the distance found for optimal speckle reduction in [10]. In all cases, the number of averaged spectra is set to  $N = 12$ , and 2 000 tomogram lines are produced. The results are shown in Fig. 10. The complex averaging result shows high speckle contrast and is not suited for speckle reduction. Both magnitude averaging and STdOCT result in speckle contrast reduction, but STdOCT offers a higher  $DR$  and  $CNR$ .

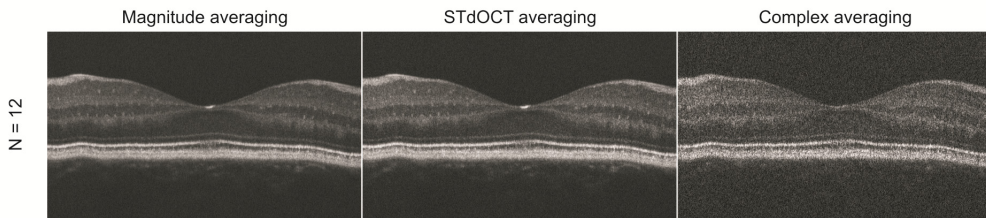


Fig. 10. In vivo imaging of a human macula lutea with speckle averaging.

## 4. Conclusions

In this work, we have analyzed the differences between three A-scan averaging techniques that can be applied to FdOCT: magnitude averaging, complex averaging, and STdOCT. For all these techniques, we calculated PDFs of the averaged A-scan magnitude as functions of the signal amplitude, standard deviation of the noise, and number of averaged A-scans. The validity of the theoretical model was confirmed by comparison with the experimental results. Additionally, we have analyzed the impact of averaging on the image quality. In the case of imaging reflecting layers, we found that complex averaging offers the highest dynamic range gain. However, in the case of imaging artificial and in vivo scattering samples, the best quality tomograms were achieved using the STdOCT approach, which is due to the fact that complex averaging is much more sensitive to decorrelation of the averaged A-scans. This effect is especially visible when averaging is applied for speckle reduction. STdOCT combines the advantages of complex and magnitude averaging techniques at the cost of an increased computation time. STdOCT offers a dynamic range increase comparable to complex averaging and a contrast-to-noise increase and speckle contrast decrease comparable to magnitude averaging. Additionally, it should be remembered that STdOCT was originally introduced for Doppler [14–16] and elastography [19] measurements and that it can provide both morphological and functional information within one computational scheme.

## Acknowledgments

This project was supported by the National Centre for Research and Development Grant No. PBS1/A9/20/2013 and by the Polish Ministry of Science and Higher Education (years 2011–2015). Maciej Wojtkowski acknowledges a EURYI grant/award funded by the European Heads of Research Councils (EuroHORCs) together with the European Science Foundation (ESF – EURYI 01/2007PL) operated by the Foundation for Polish Science. We thank Iwona Gorczynska for providing the SOCT optical setup for performing the experiments.